THE JOURNAL OF PHYSICAL CHEMISTRY C
Article
Cite This: J. Phys. Chem. C 2018, 122, 12322−12331
pubs.acs.org/JPCC

Interfacial Properties of Monolayer SnS−Metal Contacts

Sibai Li,[†,⊥] Weiji Xiao,[†,⊥] Yuanyuan Pan,[‡,⊥] Jianshu Jie,[†] Chao Xin,[∥] Jiaxin Zheng,[*,†] Jing Lu,[*,‡,§] and Feng Pan[*,†]

[†]School of Advanced Materials, Peking University Shenzhen Graduate School, Shenzhen 518055, China
[‡]State Key Laboratory for Mesoscopic Physics and Department of Physics, Peking University, Beijing 100871, China
[§]Collaborative Innovation Center of Quantum Matter, Beijing 100871, China
[∥]Jilin Key Laboratory of Solid-State Laser Technology and Application, School of Science, Changchun University of Science and Technology, Changchun 130022, China

Supporting Information

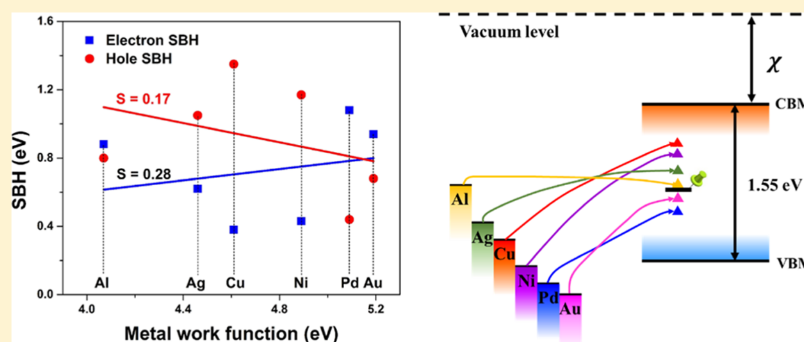

ABSTRACT: Two-dimensional semiconducting SnS is expected to have great potential for application in nanoelectronics. By using both ab initio electronic structure calculations and more reliable quantum transport simulations, we systematically explored the interfacial properties of monolayer (ML) SnS in contact with a series of metals (Ag, Al, Au, Pd, Cu, and Ni) for the first time. According to the adsorption level, three categories are found: strong adsorption is found in ML SnS−Pd and Ni contacts; medium adsorption is found in ML SnS−Cu contacts; and weak adsorption is found in ML SnS−Ag, Al, and Au contacts. Because the band structure of ML SnS is destroyed in all of the contact systems, a vertical Schottky barrier at the ML SnS−metal interface is absent. However, at the metalized-SnS/uncontacted-SnS interface in a transistor configuration, a lateral Schottky contact is always formed as a result of strong Fermi level pinning (with a pinning factor of 0.17−0.28) according to the quantum transport simulations. This work provides guidelines to design ML SnS-based devices with optimized electrode contact for high performance.

1. INTRODUCTION

Owing to their unique properties, two-dimensional (2D) materials with atomic thickness are anticipated to have an important influence on a huge diversity of applications, ranging from electronics[1−3] to high-performance sensors,[4−7] clean energy storage,[8−11] lithium-ion batteries,[12] metal−air batteries,[13] supercapacitors,[14] catalysis,[15,16] and so forth. 2D semiconductors (2DSCs) such as phosphorene[17,18] and layered metal dichalcogenides (e.g., MoS_2,[19,20] $MoSe_2$,[21,22] and WSe_2[23]) often exhibit high electrostatic gating efficiency and fewer trap states at the interface thanks to the ultrathin geometry and dangling-bond-free interface. Therefore, they are very promising to extend Moore's law down to sub-10 nm scales.[24−27]

Tin sulfide (SnS), as a compound analogue of black phosphorus, is characterized by weak interplanar van der Waals forces and strong in-plane Sn−S covalent bond,[28] as shown in Figure 1a,b. SnS nanosheets have been synthesized by physical vapor deposition,[29−31] thermodecomposition,[32] liquid-phase exfoliation (bilayer SnS),[33] and facile solvothermal method.[34] According to our previous theoretical work by HSE calculations,[35] 2D SnS has an indirect band gap that can be tuned from 1.96 eV for the monolayer (ML) to 1.44 eV for a six-layer structure. It was also found that such 2D SnS layers show high carrier mobility (~10^3 cm^2 V^{-1} s^{-1}) even superior to that of phosphorene, which renders it a promising candidate for nanoelectronic devices.

To make actual electronic and photoelectronic devices out of 2D materials, a contact with metal is often needed for injecting appropriate types of carrier into the conduction or valence band of 2D materials. The quality of the electrical contacts is as vital to the performance of the device as the semiconductor itself.[36,37] Generally, a finite Schottky barrier will appear in such contacts, leading to a decrease in the carrier injection

Received: April 8, 2018
Revised: May 21, 2018
Published: May 23, 2018

Downloaded via UNIV TOWN OF SHENZHEN on March 16, 2026 at 02:14:43 (UTC).
See https://pubs.acs.org/sharingguidelines for options on how to legitimately share published articles.

ACS Publications © 2018 American Chemical Society

DOI: 10.1021/acs.jpcc.8b03308
J. Phys. Chem. C 2018, 122, 12322−12331

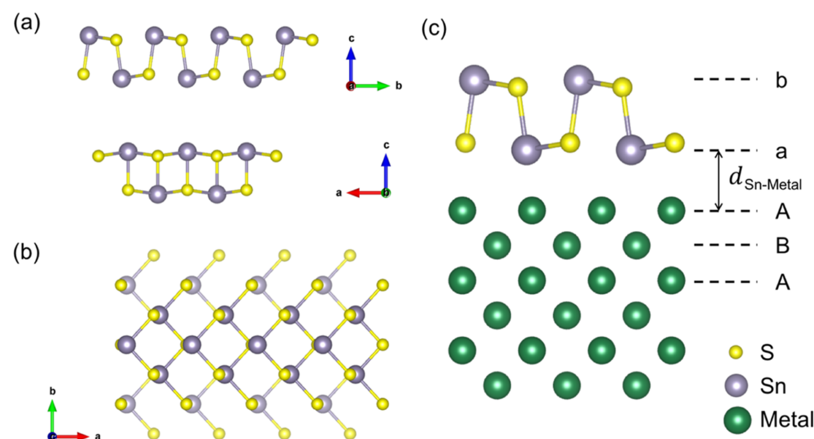

Figure 1. (a) Side and (b) top views of freestanding ML SnS. (c) Schematic diagram of initial configuration of ML SnS on the metal surface before structural optimization.

efficiency. Apparently, one of the keys to gain a high performance of a device is to reduce Schottky barrier height (SBH). However, because of the complex Fermi level pinning effect, the SBH does not simply depend on the difference between the intrinsic Fermi level (E_F) of a metal and the intrinsic conduction band minimum (CBM) or valence band maximum (VBM) of the semiconductor.[38] Besides, injecting appropriate types of carriers into the respective bands of 2D materials has to rely on the work function of contact metals on account of a lack of controllable and sustainable substitutional doping scheme.[39] Thus, it is of great importance to understand the property of 2D SnS semiconductor−metal interfaces.

In this work, the interfacial nature of ML SnS contacted with metal electrodes (Ag, Al, Au, Pd, Cu, and Ni) is systematically studied by ab initio energy band calculations and quantum transport simulations (QTSs) for the first time. In all of the systems, chemical bonds are formed between ML SnS and metal surfaces, resulting in a metallization of ML SnS and the absence of the vertical Schottky barrier at the ML SnS−metal interface. At the metalized-SnS/uncontacted-SnS interface of a field effect transistor (FET) configuration, because of the strong Fermi level pinning effect with pinning factors 0.28 for electron SBH and 0.17 for hole SBH, n-type lateral Schottky contacts are formed between ML SnS and Cu, Ni, and Ag electrodes with SBHs of 0.43, 0.15, and 0.62 eV, respectively, and p-type lateral Schottky contacts can be found between ML SnS−Al, Au, and Pd electrodes with SBHs of 0.80, 0.68, and 0.44 eV, respectively.

2. METHODOLOGY

Six metals (Ag, Al, Au, Pd, Cu, and Ni) commonly used in a transistor configuration were considered to cover a wide range of work functions. All metals in (110) orientation were chosen because they can match ML SnS well according to our analysis on the corresponding mismatches which will be mentioned below. Six layers of metal atoms were used to simulate the metal surface and to build a supercell with ML SnS adsorbed on one side of the metal surface, as shown in Figure 1c. The lattice constant of ML SnS was changed to adjust to the fixed lattice constants of the metal surface. The 1 × 2 unit cell of ML SnS matches 1 × 3 unit cells of Ag, Al, Au, and Pd, and the 1 × 3 unit cell of ML SnS matches 2 × 25 unit cells of Cu and Ni. The lattice constants of metal supercells are shown in Table 1, whereas the lattice constants of 1 × 1 unit cell of ML SnS are a = 4.02 Å and b = 4.44 Å. The corresponding mismatches are about 2% in all of the systems except the ML SnS−Pd system where the mismatch is 5.54%. The matches are reasonable because the corresponding mismatches are small. To ensure decoupling between neighboring slabs, a vacuum buffer space of at least 14 Å is set. ML SnS mainly interacts with the topmost two layers of metal atoms; therefore, the bottom four layers of metal atoms are fixed.

Table 1. Calculated Interfacial Properties of ML SnS−Metal Contacts[a]

	Ag	Al	Au	Pd	Cu	Ni
a (Å)	4.09	4.05	4.08	3.89	4.43	4.32
b (Å)	8.67	8.59	8.65	8.25	12.52	12.21
$\bar{\varepsilon}$ (%)	2.01	2.03	2.02	5.54	1.97	2.02
d_{Sn-M} (Å)	2.27	2.23	2.59	1.47	1.93	1.34
E_b (eV)	0.46	0.47	0.53	1.06	0.61	1.12
W (eV)	4.34	4.07	5.07	4.91	4.45	4.73
W_M (eV)	4.46	4.07	5.19	5.09	4.61	4.89
ΔV (eV)	0.99	0	2.67	0	0	0
w_B (Å)	0.31	0	0.70	0	0	0
T_B (%)	72.90	100	30.92	100	100	100
Φ_L^e (eV)	0.93	0.66	0	1.50	1.12	1.40
Φ_L^h (eV)	0.62	0.89	0	0.05	0.43	0.15
$\Phi_{L,T}^e$ (eV)	0.62	0.88	0.94	1.08	0.38	0.43
$\Phi_{L,T}^h$ (eV)	1.05	0.80	0.68	0.44	1.35	1.17
E_g^{tran} (eV)	1.67	1.68	1.62	1.52	1.73	1.60

[a] a and b are the lattice constants of metal supercells. $\bar{\varepsilon}$ is the lattice mismatch. The equilibrium interlayer distance d_{Sn-M} is defined as the average distance from the topmost layer metal atoms to the bottom layer Sn atoms in the vertical direction of the interface. E_b is the binding energy. W_M and W are the work functions for clean metal surface and adsorbed ML SnS−metal system, respectively. ΔV, w_B, and T_B are the tunneling barrier height, the fwhm of the potential barrier, and tunneling possibility, respectively. Φ_L^e (Φ_L^h) and $\Phi_{L,T}^e$ ($\Phi_{L,T}^h$) are the SBH obtained by WFA and QTS of electron (hole) in the lateral direction, respectively. E_g^{tran} is the transport gap, which is defined as the summary of the electron and hole lateral SBHs, that is, $E_g^{tran} = \Phi_{L,T}^e + \Phi_{L,T}^h$.

Structure optimization and electronic property calculation were performed using the Vienna ab initio simulation package[40,41] based on generalized gradient approximation (GGA)[42] to density functional theory (DFT).[43] The Perdew−Burke−Ernzerhof (PBE)[44] exchange correlation and a plane-wave representation for the wave function with a cutoff

DOI: 10.1021/acs.jpcc.8b03308
J. Phys. Chem. C 2018, 122, 12322−12331

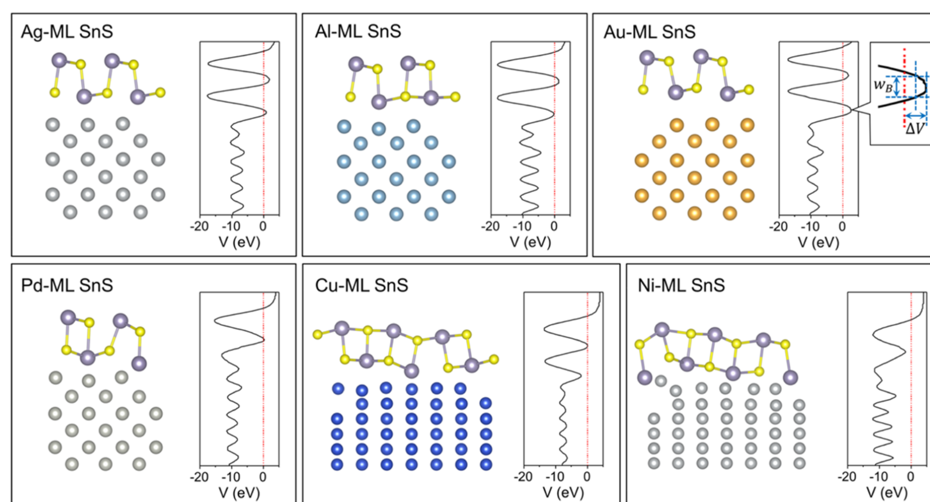

Figure 2. Side view of the optimized structures and average electrostatic potentials normal to the interface of ML SnS−Ag, Al, Au, Pd, Cu, and Ni systems. ΔV is the height of the barrier and w_B is the fwhm of the potential barrier. The Fermi level is set to zero.

of 500 eV were used. The work functions of the ML SnS−Pd system and pure Pd metal obtained by standard PBE and PBE + U methods are almost the same according to our test (Table S1). Thus, the Hubbard U was not adopted in following calculations. The maximum residual of force during geometry optimization was less than 0.01 eV/Å, and energies are converged to within 1×10^{-5} eV per atom. The Monkhorst−Pack[45] k-point mesh was sampled with a separation of about 0.02 Å^{-1} in the Brillouin zone during the relaxation and electronic calculation periods. The work functions for adsorbed ML SnS−metal systems given by spin-polarized and spin-unpolarized calculations are almost the same (Table S2). Therefore, the spin-unpolarized configuration is used for the following calculations. Many schemes and algorithms have been proposed to include van der Waals interactions.[46] One widely used approach is the vdW density functional (vdW-DF) method made by a proper choice of exchange functional.[47] Another promising approach is dispersion-corrected DFT-D in which an atom pairwise potential is added to a standard DFT result.[48] Here, van der Waals interaction is taken into account with the vdW-DF level of optB88 exchange functional (optB88-vdW),[49] which does not depend on external input parameters and yielded reasonable results in the calculation of phosphorene−metal contacts.[50] DFT-D2 and DFT-D3 give similar results according to our tests on structure optimization (Table S3).

ML SnS transistors of two terminals are built to explore the transport properties. The contacted ML SnS−metal interfaces are as electrodes, and 5 nm ML SnS is as the channel. In the light of our previous experiences, a 5 nm channel is enough to obtain the SBH of 2DSC FETs. Left and right electrodes are semi-infinite. The transmission spectrums and local device density of states (LDDOS) of these transistors are calculated by using DFT coupled with the nonequilibrium Green's function method, which is implemented in the Atomistix ToolKit (ATK) 2016 package. The GGA of the PBE form to the exchange−correlation functional and double-ζ, plus polarized basis set is used. The cutoff energy of real-space mesh is 75 hartree, and the temperature is set at 300 K. Monkhorst Pack $70 \times 1 \times 4$ and $70 \times 1 \times 1$ k-point grids are applied for electrodes and central region, respectively. Periodic-type boundary conditions are applied in the ML SnS plane vertical to the source-to-drain directions. The Neumann boundary condition is used out of the ML SnS plane and in the vacuum for the direction vertical to the source-to-drain direction, and it corresponds to a zero electric field at the boundary of the computational box. In the source-to-drain direction, the boundary condition for the electrostatic potential is decided by the electrostatic potential of the electrodes, matching the Dirichlet boundary conditions. The transmission coefficient is $T^{k_\parallel}(E)$ [$k_\parallel$ is a reciprocal lattice vector along a surface-parallel direction (orthogonal to the transmission direction) in the irreducible Brillouin zone (IBZ)] and is calculated as

$$T^{k_\parallel}(E) = \mathrm{Tr}[\Gamma_{\mathrm{L}}^{k_\parallel}(E) G^{k_\parallel}(E) \Gamma_{\mathrm{R}}^{k_\parallel}(E) G^{k_\parallel \dagger}(E)]$$

where $G^{k_\parallel}(E)(G^{k_\parallel \dagger}(E))$ is the retarded (advanced) Green's function and $\Gamma_{\mathrm{L/R}}^{k_\parallel}(E) = \mathrm{i}(\Sigma_{\mathrm{L/R}}^{r,k_\parallel} - \Sigma_{\mathrm{L/R}}^{a,k_\parallel})$ is the level broadening because of the left and right electrodes expressed in terms of the electrode self-energies $\Sigma_{\mathrm{L/R}}^{r,k_\parallel}$, which reflects the influence of the electrodes on the scattering region. The transmission function at a given energy $T(E)$ is averaged over different $k_\parallel$ in the IBZ.

3. RESULTS AND DISCUSSION

3.1. Geometry and Stability of ML SnS−Metal Interfaces. The calculated primary parameters of ML SnS−metal contacts are listed in Table 1. The binding energy E_b of the ML SnS−metal contact is defined as

$$E_b = (E_{\mathrm{SnS}} + E_{\mathrm{M}} - E_{\mathrm{SnS-M}})/N_{\mathrm{Sn}}$$

where E_{SnS}, E_{M}, and $E_{\mathrm{SnS-M}}$ are the relaxed energies for pristine ML SnS, the clean metal surface, and the combined system, respectively, and N_{Sn} is the number of Sn atoms in a supercell. The equilibrium interlayer distance $d_{\mathrm{Sn-M}}$ is defined as the average distance from the topmost layer metal atoms to the bottom layer Sn atoms in the vertical direction of the interface, as shown in Figure 1c. According to the bonding level, three categories of ML SnS−metal interfaces are classified. Weak bonding is formed for ML SnS−Ag, Al, and Au interfaces with smaller binding energy of $0.46 \leq E_b \leq 0.53$ eV and larger interlayer distance of $2.23 \leq d_{\mathrm{Sn-M}} \leq 2.59$ Å, medium bonding is formed for the ML SnS−Cu interface with a modest binding energy of 0.61 eV and an interlayer distance of 1.93 Å, and

DOI: 10.1021/acs.jpcc.8b03308
J. Phys. Chem. C 2018, 122, 12322−12331

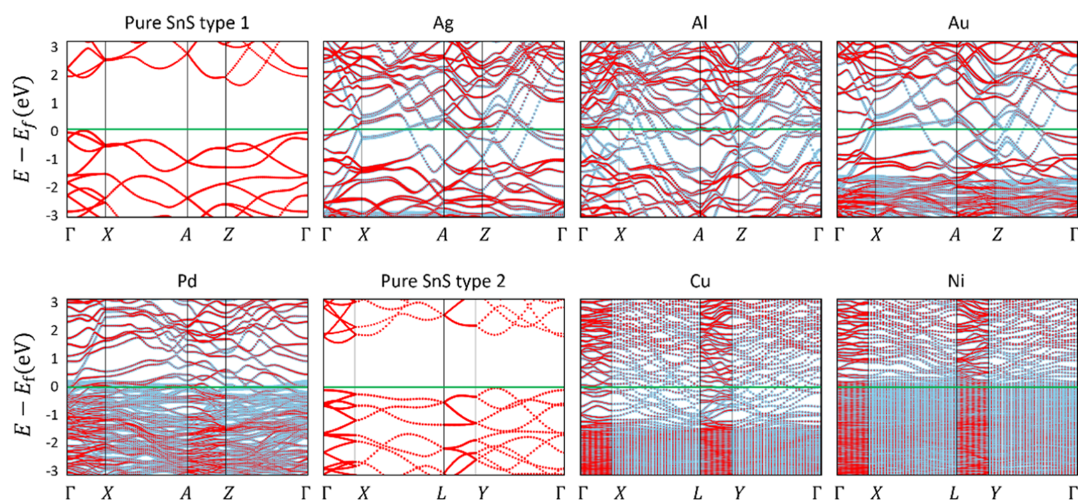

Figure 3. Band structures of ML SnS and ML SnS on Ag, Al, Au, Pd, Cu, and Ni surfaces. The Fermi level (green line) is set to zero. Light blue line: band structures of the interfacial systems; red line: band structures of ML SnS. The line width is proportional to the weight. The band structures of freestanding ML SnS are calculated in 1 × 2 (type 1) and 1 × 3 (type 2) supercells. The high symmetry points for type 1 supercell are Γ (0, 0, 0), X (0, 0.5, 0), A (0.5, 0.5, 0), and Z (0.5, 0, 0). The high symmetry points for type 2 supercell are Γ (0, 0, 0), X (0, 0.5, 0), L (0.5, 0.5, 0), and Y (0.5, 0, 0).

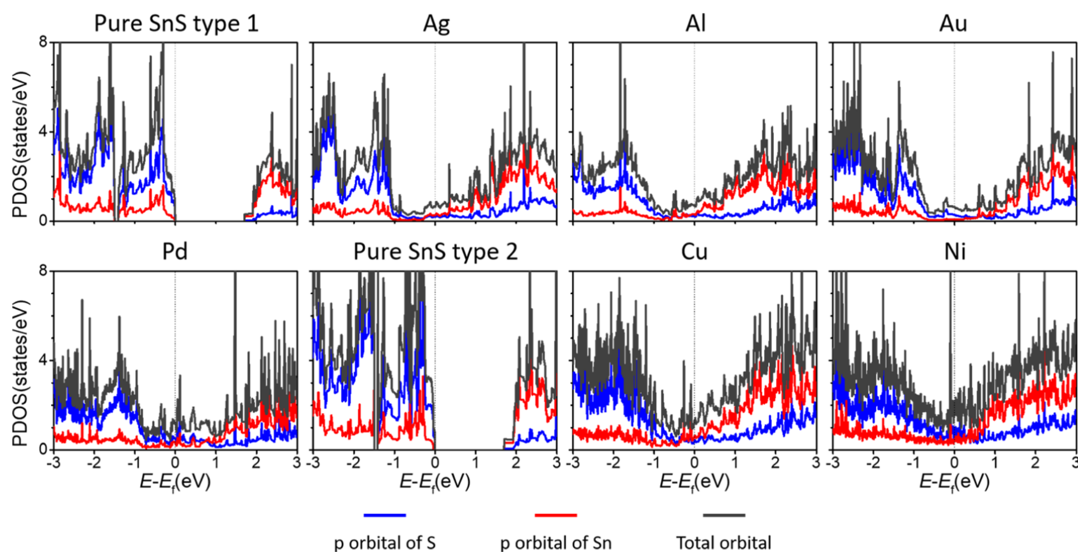

Figure 4. PDOS (density of states on specified orbitals) of pure ML SnS and ML SnS on the Ag, Al, Au, Pd, Cu, and Ni surfaces at the DFT level. The Fermi level is at zero energy. The PDOS of pure ML SnS is calculated in 1 × 2 (type 1) and 1 × 3 (type 2) supercells.

strong bonding is formed for ML SnS−Pd and Ni interfaces with larger binding energy of $1.06 \leq E_b \leq 1.12$ eV and smaller interlayer distance of $1.34 \leq d_{Sn-M} \leq 1.47$ Å. As shown in Figure 2, the shape of ML SnS changes little in weak bonding systems (ML SnS−Ag, Al, and Au), while showing an obvious deformation when contacting with Pd, Ni, and Cu.

3.2. Ab Initio Electronic Structure Calculations. The band structures of pure ML SnS and the interfacial systems are shown in Figure 3. The pure ML SnS shows an indirect band gap of 1.55 eV, close to the former GGA result but smaller than the former HSE value (1.96 eV).[35] As Figure 3 shows, the ML SnS-derived bands always cross the Fermi level for all of the interfacial systems, which means that ML SnS undergoes metallization because of the strong hybridization. However, the hybridization degree for the band structures of ML SnS on metals varies: the band hybridizations of ML SnS on Cu, Ni, and Pd electrodes are more intense than those on Al, Ag, and Au electrodes, which is in accordance with the binding energies. For comparison, the band structures of ML $MoSe_2$ absorbed on Ag and Al are still distinguishable.[38] These facts indicate that ML SnS is chemically adsorbed on metal surface and strong covalent bonds are formed.

The calculated partial density of states (PDOS) on Sn and S orbitals for ML SnS−metal systems is shown in Figure 4 and is helpful for deeper understanding of the metallization degree. A large portion of Sn and S states appear in the original band gap of pure ML SnS, especially the Sn p orbital and S p orbital, which reflects the strong band hybridization and the covalent bond formation between the metal and the Sn and S p orbitals. The PDOS at the Fermi level (E_F) is not zero, indicating that ML SnS undergoes metallization when contacted with metals. The PDOS of Cu, Ni, and Pd is larger than those of Ag, Al, and Au at E_F, reflecting a higher metallization degree on Cu, Ni, and Pd, a result consistent with their higher hybridization degree. The total electron distribution of ML SnS−metal interfacial systems, which can reflect the interaction between ML SnS and

DOI: 10.1021/acs.jpcc.8b03308
J. Phys. Chem. C 2018, 122, 12322−12331

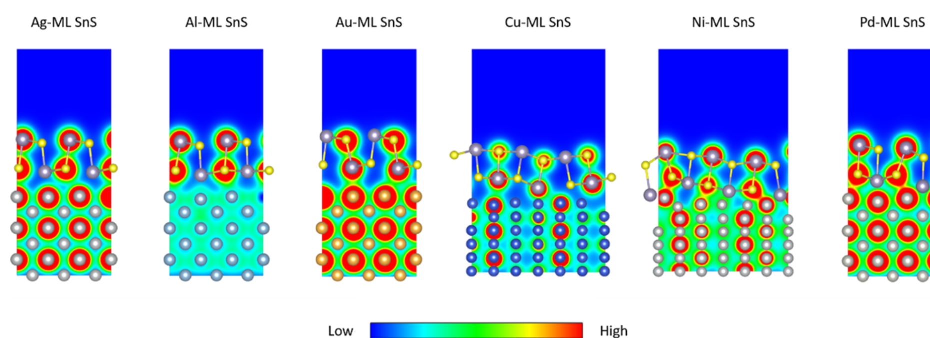

Figure 5. Contour plots of total electron distribution of the ML SnS−metal interfacial systems.

metal surfaces, is shown in Figure 5. The electron accumulation in the ML SnS−metal interfaces indicates the formation of a covalent bond between ML SnS and metal surfaces again. The electron accumulation at ML SnS−Ni and Pd interfaces is more apparent than that at ML SnS−Ag, Al, Au, and Cu interfaces, as is in line with their bonding and hybridization levels. Furthermore, Bader charge analysis[51−54] can give quantitative results of charge on S and Sn atoms. As listed in Table 2, the average charge on S in strong bonding systems (ML SnS−Pd and Ni) is smaller than that in weak or medium bonding systems (ML SnS−Ag, Au, Al, and Cu). The less charge accumulated on S atoms, the stronger the covalent bond between S and metal. The Bader charge results are in accordance with the hybridization degree. The different hybridization degrees can be attributed to the different occupied levels of the d-orbital of metals. Group 11 elements Cu ($3d^{10}4s^1$), Ag ($4d^{10}5s^1$), and Au ($5d^{10}6s^1$) have fully filled d-orbital, and p-block element Al ($3s^2p^1$) has unfilled d-orbitals, so they only form one covalent bond with the orbitals of the contacted S atoms. Ni atom ($3d^84s^2$) has partially filled d-orbital and half-filled s-orbital. Isolated Pd atom ($4d^{10}$) has fully filled d-orbital, but the electron distribution of Pd is similar to Ni and Pt in the solid form.[55,56] Thus, additional d-orbital-related covalent bond is formed between Ni/Pd and ML SnS, which makes the binding energies of ML SnS−Ni and Pd larger than that of other systems.

Table 2. Bader Charges on S and Sn Atoms in the ML SnS−Metal Contacts[a]

atom	Ag	Al	Au	Pd	Cu	Ni
S1	6.91	7.13	6.88	6.76	6.91	6.83
S2	6.94	6.93	6.91	6.92	6.91	6.88
S3	6.90	7.13	6.90	6.74	6.89	6.82
S4	6.94	6.94	6.93	6.86	6.91	6.91
S5					6.82	6.72
S6					6.93	6.90
S	6.93	7.03	6.91	6.82	6.89	6.84
Sn1	13.06	13.06	13.06	13.09	13.08	13.13
Sn2	13.08	13.34	12.92	12.82	13.05	12.94
Sn3	13.06	13.07	13.06	13.08	13.08	13.06
Sn4	13.09	13.17	12.95	13.01	13.33	13.08
Sn5					13.06	13.09
Sn6					13.08	13.29
Sn	13.07	13.16	13.00	13.00	13.11	13.11

[a]S and Sn mean average of all of the S and Sn atoms.

Figure 6a shows the schematic drawing of a ML SnS FET. Schottky barriers may exist at either of two different interfaces of a ML SnS−metal interfacial system: one is between metal and ML SnS contacted surface (labeled interface B) and the other is between the interfacial system and channel SnS (labeled interface D). If the contacted ML SnS becomes metallization, the Schottky barrier is absent at interface B and only can appear at interface D. It should be noted that the tunneling barrier would exist at interface B when electrons or holes cross the gap between metal and ML SnS, though there is no Schottky barrier at interface B.

Because of the high hybridization degree, there is no vertical SBH at interface B. Lateral SBH at interface D can be attained by work function approximation (WFA). The WFA method calculates the energy differences between E_F of the interfacial system and the CBM or VBM of channel pure ML SnS. Figure 7 shows the line-up of the metal Fermi level with the electronic bands of ML SnS. The calculated work functions of ML SnS are 3.41 eV for type 1 and 3.33 eV for type 2, respectively. It is found that after contacting with ML SnS, the work function of the interfacial systems is larger than that of the pure metal except the ML SnS−Al system. As shown in Figure 8, according to WFA, ML SnS forms p-type Schottky contacts with Pd, Ni, Cu, Ag, and Al with SBHs Φ_L^h = 0.05, 0.15, 0.43, 0.62, and 0.89 eV, respectively, whereas it forms Ohmic contacts with Au; for the interfacial systems, E_F is lower than the VBM of channel ML SnS. SBH as small as 0.05 eV indicates quasi-Ohmic contact between ML SnS and Pd.

The tunneling barrier is another important character of a semiconductor−metal contact. The potential profiles at the vertical ML SnS−metal interfaces are shown in Figure 2. The barrier height of ML SnS−Ag and Au is 0.99 and 2.67 eV, respectively. A square potential barrier is adopted to estimate the real potential barrier. The tunneling probability T_B is defined by[57]

$$T_B = \exp\left(-2\frac{\sqrt{2m\Delta V}}{\hbar} \times w_B\right)$$

where m is the mass of the free electron, $\hbar$ is the reduced Planck constant, ΔV is the height of the barrier, and w_B is the full width at half-maximum (fwhm) of the potential barrier (Figure 2). The results of T_B values are 30.92, 72.90, 100, 100, 100, and 100% for ML SnS−Ag, Au, Cu, Al, Pd, and Ni contacts, respectively. The tunneling barrier vanishes in strong and medium bonding systems such as ML SnS−Cu, Ni, and Pd, whereas appears in weaker bonding systems including ML SnS−Ag and Au. The absence of tunneling barrier makes the electron or hole transfer freely.

3.3. Quantum Transport Simulations. To further accurately describe the lateral SBH, we build a two-terminal

DOI: 10.1021/acs.jpcc.8b03308
J. Phys. Chem. C 2018, 122, 12322−12331

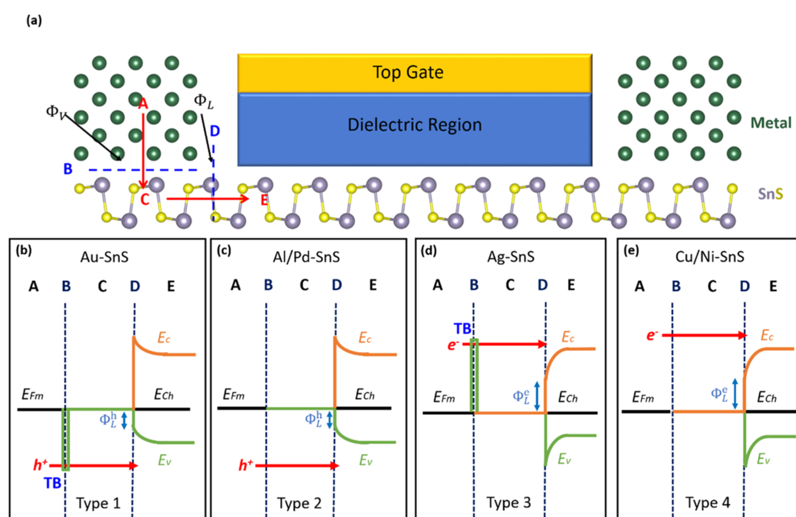

Figure 6. (a) Schematic diagram of a ML SnS FET. Schematic cross-sectional view of a typical metal contact to intrinsic ML SnS channel. (A,C,E) denotes three regions, whereas (B,D) are the two interfaces separating them. Red rows show the pathway (A → B → C → D → E) of electron or hole injection from contact metal (A) to the ML SnS channel (E). (b–e) Three possible band diagrams of the ML SnS FETs in view of Schottky barriers and tunneling barrier, depending on the type of metal electrode. E_{Fm} and E_{Ch} denote the Fermi level of the interfacial systems and channel ML SnS, respectively.

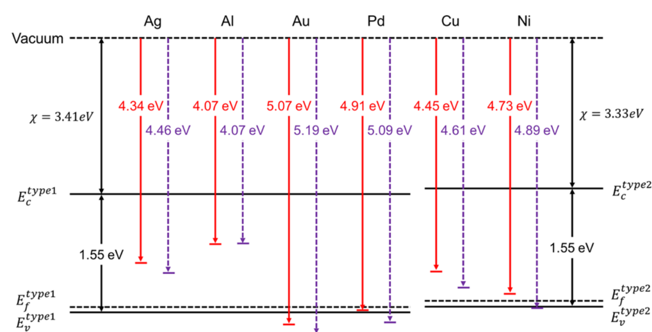

Figure 7. Line-up of the work functions of the interfacial systems with the electronic band of channel ML SnS in terms of separate electronic energy band calculations. The purple dashed and red solid lines present the work function of the pure metal and ML SnS–metal systems, respectively.

ML SnS transistor, as shown in Figure 7a, and calculate the properties of the transistors by using the ab initio QTSs. The channel length is 5 nm. Zero-bias and zero-gate voltage LDDOS and transmission spectra of the ML SnS transistors with Cu, Ag, Ni, Al, Au, and Pd as electrodes are plotted in Figure 8. LDDOS gives the energy band in the real space of the ML SnS transistors. The band edges of the channel ML SnS with Ag and Au as electrodes are flat as the free-standing ML SnS, whereas those with Cu, Ni, Al, and Pd as electrodes are tilted. The tilting of the band edges results from the distorted contacted structures shown in Figure 2 and the asymmetric structures between left and right electrodes. At the source/drain–channel interfaces, the lateral electron (hole) SBH is defined as the energy difference between the Fermi level and the CBM (VBM) of the channel ML SnS. For the transistors with asymmetric electrodes, the lateral electron (hole) SBH is the average of the electron (hole) SBH at the source–channel interfaces and that at the drain–channel interface.

ML SnS forms n-type lateral Schottky contact with Cu, Ni, and Ag electrodes with electron SBHs of 0.38, 0.43, and 0.62 eV, respectively, whereas it forms p-type lateral Schottky contact with Pd, Au, and Al electrodes with hole SBHs of 0.44, 0.68, and 0.80 eV, respectively. There are apparent metal-induced gap states (MIGS) in the gap of the ML SnS channel, which often cause Fermi level pinning and will be discussed later. The transport gap $E_{\mathrm{g}}^{\mathrm{tran}}$ is defined as the summary of electron and hole lateral SBHs, that is, $E_{\mathrm{g}}^{\mathrm{tran}} = \Phi_{\mathrm{L,T}}^{\mathrm{e}} + \Phi_{\mathrm{L,T}}^{\mathrm{h}}$. The transport gaps are 1.73, 1.60, 1.67, 1.68, 1.62, and 1.52 eV for ML SnS transistors with metals Cu, Ni, Ag, Al, Au, and Pd as electrodes, respectively. These transport gaps are consistent with the intrinsic band gap of 1.55 eV of the infinite ML SnS.

3.4. Comparison of the Lateral Schottky Barriers between the Two Methods. We have compared the lateral electron/hole SBH of the ML SnS transistors obtained by the QTSs and the WFA in Figure 9. The type and height of the Schottky barrier by these two methods are apparently different from each other. Under the WFA, ML SnS forms p-type contacts with all metals except with Al, especially it forms p-type Ohmic contacts with Au. By contrast, under the QTS, ML forms n-type Schottky contact with Cu, Ni, and Ag, whereas it forms p-type Schottky contacts with Pd, Au, and Al. The WFA prefers a smaller hole SBH, such as the hole SBHs with Pd, Ag, Cu, and Ni are 0.35, 0.43, 0.88, and 1.02 eV lower than that by using the QTSs, respectively. The significant differences between these two methods originate from the fact that the WFA deals with the electrode and the channel separately, and thus, it ignores the coupling between these two regions. While the QTS treats the electrode and the channel as a whole and includes the coupling between the two regions. The ignoration of such a coupling at the interface generally brings about an underestimation of the SBH, as revealed in previous works.[50,58–60]

In view of tunneling barriers and Schottky barriers given by the QTSs, four types of ML SnS–metal contact are identified, as shown in Figure 6b–f. ML SnS forms the type 1 contact with the Au electrode, in which ML SnS forms p-type Schottky contact with Au at lateral interface D and tunneling barrier appears at vertical interface B. ML SnS forms the type 2 contact with Al and Pd, in which holes only face a p-type Schottky barrier at the lateral interface D. In type 3, electrons face both an n-type Schottky barrier at the lateral interface D and a

DOI: 10.1021/acs.jpcc.8b03308
J. Phys. Chem. C 2018, 122, 12322–12331

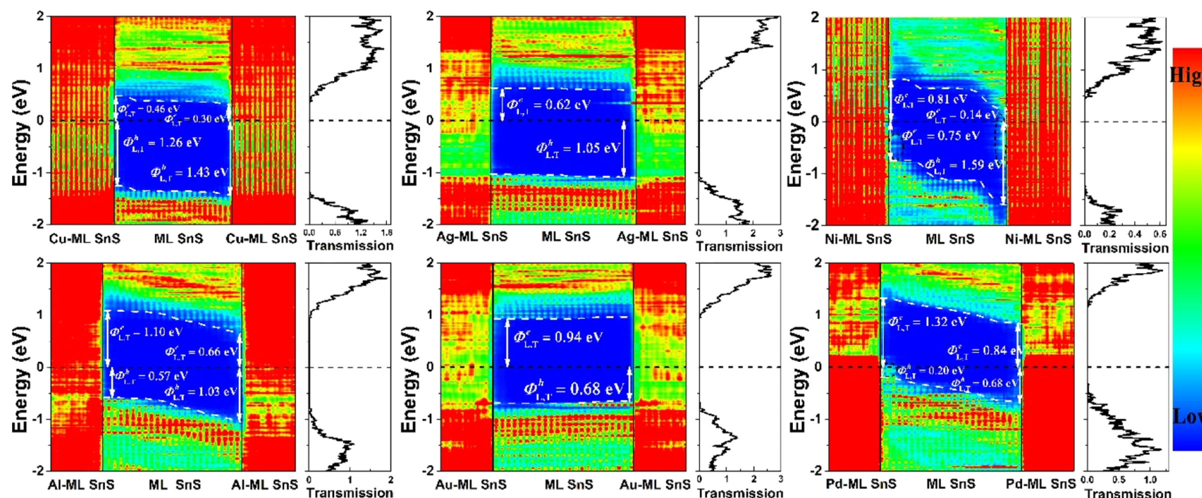

Figure 8. LDDOS and transmission spectra of ML SnS FETs with Cu, Ag, Ni, Al, Au, and Pd as electrodes. The channel length is set as 5 nm with zero-bias and zero-gate voltages. The Fermi level is represented by black dashed line and is set at zero. The white dashed lines represent the band edge of ML SnS in the channel. The black solid line indicates the boundary of the ML SnS source/drain electrode. $\Phi^{e}_{L,T}$ and $\Phi^{h}_{L,T}$ denote the lateral electron and hole SBHs, respectively. The color scale is shown in the right. The black circles denote the interfacial states in the band gap of channel ML SnS.

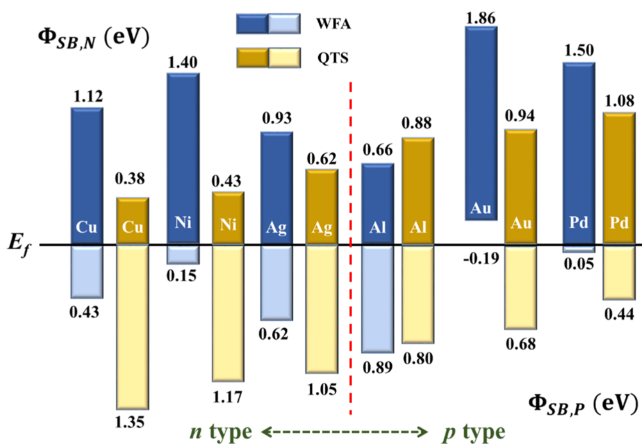

Figure 9. Comparison of the lateral hole/electron SBHs at ML SnS−Pd, Ni, Cu, Ag, Al, and Au interfaces by using DFT WFA and the QTSs.

tunneling barrier at vertical interface B. ML SnS forms an n-type Schottky contact at lateral interface D, and tunneling barrier vanishes at vertical interface B.

To further uncover the dependence of the lateral SBH on the work function of the intrinsic metal and the Fermi level pinning, we plot the SBH versus the metals work function in Figure 10a. The pinning factor is defined as the slope $S = d\Phi^{e/h}_{L,T}/dW_M$, where W_M is the work function of the intrinsic metals. The pinning factor varies between $S = 0$ for strongly pinned interfaces (Bardeen limit) and $S = 1$ for unpinned interfaces (Schottky limit).[61,62] The pinning factors for electron and hole are roughly estimated to be 0.28 and 0.17, respectively, which are comparable with the calculated values in other 2DSC, such as black phosphorene (0.28), ML bismuthene (0.12), ML MoS_2 (0.30), and arsenene (0.33).[50,56,58−60,63−65] The small pinning factor indicates a strong Fermi level pinning, and the Fermi level is pinned around the center of the band gap, as illustrated in Figure 10b.

4. CONCLUSIONS

The interfacial properties of ML SnS contacting with a series of metals (Ag, Al, Au, Pd, Cu, and Ni) were investigated systematically by using both ab initio electronic structure calculations and more reliable QTSs. It is found that group 10 metals Pd and Ni show strong absorption, whereas group 11

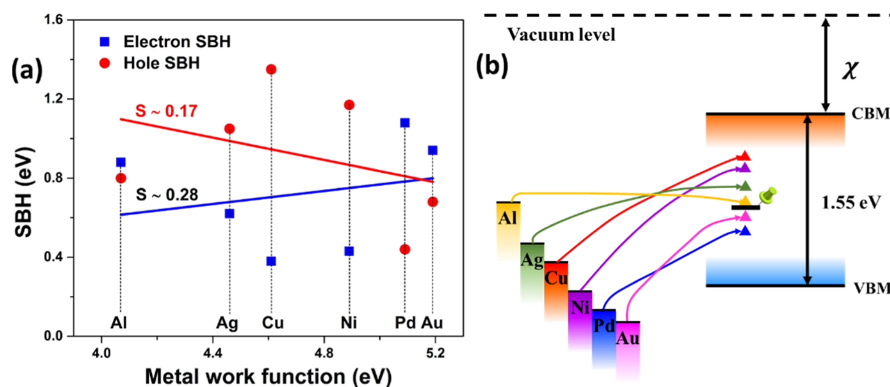

Figure 10. (a) Calculated electron and hole SBHs as a function of the work function of the intrinsic metals. S is the pinning factor according to the Schottky−Mott rule. (b) Schematic figures of the Fermi level pinning in the ML SnS transistors.

DOI: 10.1021/acs.jpcc.8b03308
J. Phys. Chem. C 2018, 122, 12322−12331

Cu, Ag, Au, and p-block metal Al show weak or medium absorption with ML SnS. Because of the metallization of ML SnS in all of the contact systems, a vertical Schottky barrier at the ML SnS–metal interface is absent. However, a lateral Schottky contact can still exist in ML SnS–metal systems at the metalized-SnS/uncontacted-SnS interface for real FET devices. The ab initio band calculations and QTSs give reversed carrier polarity when Cu, Ni, and Ag are used as electrodes. Furthermore, the ML SnS FET with a Au electrode changes from Ohmic contact (the electronic band structure calculations) to p-type Schottky contact with a large hole SBH of 0.68 eV. On the basis of the QTSs, n-type Schottky contacts are formed between ML SnS and Cu, Ni, and Ag electrodes with SBHs of 0.43, 0.15, and 0.62 eV, respectively, and p-type Schottky contacts can be found between ML SnS–Al, Au, and Pd electrodes with SBHs of 0.80, 0.68, and 0.44 eV, respectively. Our further study also shows that the tunneling barrier vanishes in ML SnS–Cu, Al, Ni, and Pd systems, leading to enhanced carrier transfer performance. This article provides a theoretical guideline for designing ML SnS-based nanoelectronic devices with high performance.

■ ASSOCIATED CONTENT

Supporting Information

The Supporting Information is available free of charge on the ACS Publications website at DOI: 10.1021/acs.jpcc.8b03308.

Comparison of the work functions for clean metal surface and ML SnS–Pd system calculated by PBE and PBE + *U*; comparison of the work functions for ML SnS–metal systems given by spin-polarized and spin-unpolarized calculations; comparison of the equilibrium interlayer distances between ML SnS and the metal surfaces obtained by vdW-DF, DFT-D2, and DFT-D3 methods; and the 2D Brillouin zone of ML SnS for the (a) 1 × 2 (type 1) and (b) 1 × 3 (type 2) supercells (PDF)

■ AUTHOR INFORMATION

Corresponding Authors

*E-mail: zhengjx@pkusz.edu.cn (J.Z.).
*E-mail: jinglu@pku.edu.cn (J.L.).
*E-mail: panfeng@pkusz.edu.cn (F.P.).

ORCID

Sibai Li: 0000-0002-4301-132X
Feng Pan: 0000-0002-8216-1339

Author Contributions

⊥S.L., W.X., and Y.P. contributed equally to this work.

Notes

The authors declare no competing financial interest.

■ ACKNOWLEDGMENTS

This work was financially supported by National Materials Genome Project (2016YFB0700600), the National Natural Science Foundation of China (nos. 21603007, 51672012, and 11674005), and Shenzhen Science and Technology Research Grant (nos. JCYJ20150729111733470 and JCYJ20151015162256516).

■ REFERENCES

(1) Zhang, Y.; Tan, Y.-W.; Stormer, H. L.; Kim, P. Experimental Observation of the Quantum Hall Effect and Berry's Phase in Graphene. *Nature* **2005**, *438*, 201.

(2) Morozov, S. V.; Novoselov, K. S.; Katsnelson, M. I.; Schedin, F.; Elias, D. C.; Jaszczak, J. A.; Geim, A. K. Giant Intrinsic Carrier Mobilities in Graphene and Its Bilayer. *Phys. Rev. Lett.* **2008**, *100*, 016602.

(3) Fang, H.; Tosun, M.; Seol, G.; Chang, T. C.; Takei, K.; Guo, J.; Javey, A. Degenerate N-Doping of Few-Layer Transition Metal Dichalcogenides by Potassium. *Nano Lett.* **2013**, *13*, 1991–1995.

(4) Yuan, W.; Shi, G. Graphene-Based Gas Sensors. *J. Mater. Chem. A* **2013**, *1*, 10078–10091.

(5) Schedin, F.; Geim, A. K.; Morozov, S. V.; Hill, E. W.; Blake, P.; Katsnelson, M. I.; Novoselov, K. S. Detection of Individual Gas Molecules Adsorbed on Graphene. *Nat. Mater.* **2007**, *6*, 652.

(6) Hussain, T.; Hankel, M.; Searles, D. J. Improving Sensing of Sulfur-Containing Gas Molecules with Zno Monolayers by Implanting Dopants and Defects. *J. Phys. Chem. C* **2017**, *121*, 24365–24375.

(7) Hussain, T.; Vovusha, H.; Kaewmaraya, T.; Amornkitbamrung, V.; Ahuja, R. Adsorption Characteristics of DNA Nucleobases, Aromatic Amino Acids and Heterocyclic Molecules on Silicene and Germanene Monolayers. *Sens. Actuators, B* **2018**, *255*, 2713–2720.

(8) Liao, J.-H.; Zhao, Y.-J.; Yang, X.-B. Controllable Hydrogen Adsorption and Desorption by Strain Modulation on Ti Decorated Defective Graphene. *Int. J. Hydrogen Energy* **2015**, *40*, 12063–12071.

(9) Lee, H.; Ihm, J.; Cohen, M. L.; Louie, S. G. Calcium-Decorated Graphene-Based Nanostructures for Hydrogen Storage. *Nano Lett.* **2010**, *10*, 793–798.

(10) Hussain, T.; Hankel, M.; Searles, D. J. Graphenylene Monolayers Doped with Alkali or Alkaline Earth Metals: Promising Materials for Clean Energy Storage. *J. Phys. Chem. C* **2017**, *121*, 14393–14400.

(11) Farokh Niaei, A. H.; Hussain, T.; Hankel, M.; Searles, D. J. Sodium-Intercalated Bulk Graphdiyne as an Anode Material for Rechargeable Batteries. *J. Power Sources* **2017**, *343*, 354–363.

(12) Tian, L.-L.; Li, S.-B.; Zhang, M.-J.; Li, S.-K.; Lin, L.-P.; Zheng, J.-X.; Zhuang, Q.-C.; Amine, K.; Pan, F. Cascading Boost Effect on the Capacity of Nitrogen-Doped Graphene Sheets for Li- and Na-Ion Batteries. *ACS Appl. Mater. Interfaces* **2016**, *8*, 26722–26729.

(13) Tian, L.-L.; Yang, J.; Weng, M.-Y.; Tan, R.; Zheng, J.-X.; Chen, H.-B.; Zhuang, Q.-C.; Dai, L.-M.; Pan, F. Fast Diffusion of O_2 on Nitrogen-Doped Graphene to Enhance Oxygen Reduction and Its Application for High-Rate Zn–Air Batteries. *ACS Appl. Mater. Interfaces* **2017**, *9*, 7125–7130.

(14) Huang, Y.; Zhao, Y.; Gong, Q.; Weng, M.; Bai, J.; Liu, X.; Jiang, Q.; Wang, J.; Wang, D.; Shao, Y.; et al. Experimental and Correlative Analyses of the Ageing Mechanism of Activated Carbon Based Supercapacitor. *Electrochim. Acta* **2017**, *228*, 214–225.

(15) Kong, X.-K.; Chen, C.-L.; Chen, Q.-W. Doped Graphene for Metal-Free Catalysis. *Chem. Soc. Rev.* **2014**, *43*, 2841–2857.

(16) Mao, K.; Li, L.; Zhang, W.; Pei, Y.; Zeng, X. C.; Wu, X.; Yang, J. A Theoretical Study of Single-Atom Catalysis of Co Oxidation Using Au Embedded 2d H-Bn Monolayer: A Co-Promoted O_2 Activation. *Sci. Rep.* **2014**, *4*, 5441.

(17) Li, L.; Yu, Y.; Ye, G. J.; Ge, Q.; Ou, X.; Wu, H.; Feng, D.; Chen, X. H.; Zhang, Y. Black Phosphorus Field-Effect Transistors. *Nat. Nanotechnol.* **2014**, *9*, 372.

(18) Das, S.; Zhang, W.; Demarteau, M.; Hoffmann, A.; Dubey, M.; Roelofs, A. Tunable Transport Gap in Phosphorene. *Nano Lett.* **2014**, *14*, 5733–5739.

(19) Kim, S.; Konar, A.; Hwang, W.-S.; Lee, J. H.; Lee, J.; Yang, J.; Jung, C.; Kim, H.; Yoo, J.-B.; Choi, J.-Y.; et al. High-Mobility and Low-Power Thin-Film Transistors Based on Multilayer MoS_2 Crystals. *Nat. Commun.* **2012**, *3*, 1011.

(20) Sarkar, D.; Liu, W.; Xie, X.; Anselmo, A. C.; Mitragotri, S.; Banerjee, K. MoS_2 Field-Effect Transistor for Next-Generation Label-Free Biosensors. *ACS Nano* **2014**, *8*, 3992–4003.

(21) Larentis, S.; Fallahazad, B.; Tutuc, E. Field-Effect Transistors and Intrinsic Mobility in Ultra-Thin Mose2 Layers. *Appl. Phys. Lett.* **2012**, *101*, 223104.

(22) Pradhan, N. R.; Rhodes, D.; Xin, Y.; Memaran, S.; Bhaskaran, L.; Siddiq, M.; Hill, S.; Ajayan, P. M.; Balicas, L. Ambipolar Molybdenum

DOI: 10.1021/acs.jpcc.8b03308
J. Phys. Chem. C 2018, 122, 12322–12331

Diselenide Field-Effect Transistors: Field-Effect and Hall Mobilities. *ACS Nano* **2014**, *8*, 7923−7929.
(23) Fang, H.; Chuang, S.; Chang, T. C.; Takei, K.; Takahashi, T.; Javey, A. High-Performance Single Layered Wse2 P-Fets with Chemically Doped Contacts. *Nano Lett.* **2012**, *12*, 3788−3792.
(24) Ni, Z.; Ye, M.; Ma, J.; Wang, Y.; Quhe, R.; Zheng, J.; Dai, L.; Yu, D.; Shi, J.; Yang, J.; et al. Performance Upper Limit of Sub-10 nm Monolayer MoS2 Transistors. *Adv. Electron. Mater.* **2016**, *2*, 1600191.
(25) Wang, Y.; Huang, P.; Ye, M.; Quhe, R.; Pan, Y.; Zhang, H.; Zhong, H.; Shi, J.; Lu, J. Many-Body Effect, Carrier Mobility, and Device Performance of Hexagonal Arsenene and Antimonene. *Chem. Mater.* **2017**, *29*, 2191−2201.
(26) Desai, S. B.; Madhvapathy, S. R.; Sachid, A. B.; Llinas, J. P.; Wang, Q.; Ahn, G. H.; Pitner, G.; Kim, M. J.; Bokor, J.; Hu, C.; Wong, H.-S. P.; et al. MoS_2 Transistors with 1-Nanometer Gate Lengths. *Science* **2016**, *354*, 99−102.
(27) Quhe, R.; Peng, X.; Pan, Y.; Ye, M.; Wang, Y.; Zhang, H.; Feng, S.; Zhang, Q.; Shi, J.; Yang, J.; et al. Can a Black Phosphorus Schottky Barrier Transistor Be Good Enough? *ACS Appl. Mater. Interfaces* **2017**, *9*, 3959−3966.
(28) Ke, F.; Yang, J.; Liu, C.; Wang, Q.; Li, Y.; Zhang, J.; Wu, L.; Zhang, X.; Han, Y.; Wu, B.; et al. High-Pressure Electrical-Transport Properties of SnS: Experimental and Theoretical Approaches. *J. Phys. Chem. C* **2013**, *117*, 6033−6038.
(29) Xia, J.; Li, X.-Z.; Huang, X.; Mao, N.; Zhu, D.-D.; Wang, L.; Xu, H.; Meng, X.-M. Physical Vapor Deposition Synthesis of Two-Dimensional Orthorhombic Sns Flakes with Strong Angle/Temperature-Dependent Raman Responses. *Nanoscale* **2016**, *8*, 2063−2070.
(30) Kang, J.-G.; Ko, Y.-D.; Choi, K. J.; Park, J.-G.; Kim, D.-W. Fabrication of Tin Monosulfide Nanosheet Arrays Using Laser Ablation. *Appl. Phys. A* **2011**, *103*, 505−510.
(31) Kang, J.-G.; Park, J.-G.; Kim, D.-W. Superior Rate Capabilities of Sns Nanosheet Electrodes for Li Ion Batteries. *Electrochem. Commun.* **2010**, *12*, 307−310.
(32) Zhang, Y.; Lu, J.; Shen, S.; Xu, H.; Wang, Q. Ultralarge Single Crystal Sns Rectangular Nanosheets. *Chem. Commun.* **2011**, *47*, 5226−5228.
(33) Brent, J. R.; Lewis, D. J.; Lorenz, T.; Lewis, E. A.; Savjani, N.; Haigh, S. J.; Seifert, G.; Derby, B.; O'Brien, P. Tin(Ii) Sulfide (SnS) Nanosheets by Liquid-Phase Exfoliation of Herzenbergite: Iv−Vi Main Group Two-Dimensional Atomic Crystals. *J. Am. Chem. Soc.* **2015**, *137*, 12689−12696.
(34) Li, S.; Zheng, J.; Zuo, S.; Wu, Z.; Yan, P.; Pan, F. 2d Hybrid Anode Based on Sns Nanosheet Bonded with Graphene to Enhance Electrochemical Performance for Lithium-Ion Batteries. *RSC Adv.* **2015**, *5*, 46941−46946.
(35) Xin, C.; Zheng, J.; Su, Y.; Li, S.; Zhang, B.; Feng, Y.; Pan, F. Few-Layer Tin Sulfide: A New Black-Phosphorus-Analogue 2d Material with a Sizeable Band Gap, Odd−Even Quantum Confinement Effect, and High Carrier Mobility. *J. Phys. Chem. C* **2016**, *120*, 22663−22669.
(36) Allain, A.; Kang, J.; Banerjee, K.; Kis, A. Electrical Contacts to Two-Dimensional Semiconductors. *Nat. Mater.* **2015**, *14*, 1195.
(37) Léonard, F.; Talin, A. A. Electrical Contacts to One- and Two-Dimensional Nanomaterials. *Nat. Nanotechnol.* **2011**, *6*, 773.
(38) Pan, Y.; Li, S.; Ye, M.; Quhe, R.; Song, Z.; Wang, Y.; Zheng, J.; Pan, F.; Guo, W.; Yang, J.; et al. Interfacial Properties of Monolayer $MoSe_2$−Metal Contacts. *J. Phys. Chem. C* **2016**, *120*, 13063−13070.
(39) Kang, J.; Liu, W.; Sarkar, D.; Jena, D.; Banerjee, K. Computational Study of Metal Contacts to Monolayer Transition-Metal Dichalcogenide Semiconductors. *Phys. Rev. X* **2014**, *4*, 031005.
(40) Kresse, G.; Furthmüller, J. Efficient Iterative Schemes for Ab Initio Total-Energy Calculations Using a Plane-Wave Basis Set. *Phys. Rev. B: Condens. Matter Mater. Phys.* **1996**, *54*, 11169−11186.
(41) Kresse, G.; Furthmüller, J. Efficiency of Ab-Initio Total Energy Calculations for Metals and Semiconductors Using a Plane-Wave Basis Set. *Comput. Mater. Sci.* **1996**, *6*, 15−50.
(42) Perdew, J. P.; Chevary, J. A.; Vosko, S. H.; Jackson, K. A.; Pederson, M. R.; Singh, D. J.; Fiolhais, C. Atoms, Molecules, Solids, and Surfaces: Applications of the Generalized Gradient Approximation for Exchange and Correlation. *Phys. Rev. B: Condens. Matter Mater. Phys.* **1992**, *46*, 6671−6687.
(43) Jones, R. O.; Gunnarsson, O. The Density Functional Formalism, Its Applications and Prospects. *Rev. Mod. Phys.* **1989**, *61*, 689−746.
(44) Perdew, J. P.; Burke, K.; Ernzerhof, M. Generalized Gradient Approximation Made Simple. *Phys. Rev. Lett.* **1996**, *77*, 3865−3868.
(45) Monkhorst, H. J.; Pack, J. D. Special Points for Brillouin-Zone Integrations. *Phys. Rev. B: Solid State* **1976**, *13*, 5188−5192.
(46) Park, J.; Yu, B. D.; Hong, S. Van Der Waals Density Functional Theory Study for Bulk Solids with Bcc, Fcc, and Diamond Structures. *Curr. Appl. Phys.* **2015**, *15*, 885−891.
(47) Dion, M.; Rydberg, H.; Schröder, E.; Langreth, D. C.; Lundqvist, B. I. Van Der Waals Density Functional for General Geometries. *Phys. Rev. Lett.* **2004**, *92*, 246401.
(48) Grimme, S.; Antony, J.; Ehrlich, S.; Krieg, H. A Consistent and Accurate Ab Initio Parametrization of Density Functional Dispersion Correction (Dft-D) for the 94 Elements H-Pu. *J. Chem. Phys.* **2010**, *132*, 154104.
(49) Klimeš, J.; Bowler, D. R.; Michaelides, A. Chemical Accuracy for the Van Der Waals Density Functional. *J. Phys.: Condens. Matter* **2010**, *22*, 022201.
(50) Pan, Y.; Wang, Y.; Ye, M.; Quhe, R.; Zhong, H.; Song, Z.; Peng, X.; Yu, D.; Yang, J.; Shi, J.; et al. Monolayer Phosphorene−Metal Contacts. *Chem. Mater.* **2016**, *28*, 2100−2109.
(51) Tang, W.; Sanville, E.; Henkelman, G. A Grid-Based Bader Analysis Algorithm without Lattice Bias. *J. Phys.: Condens. Matter* **2009**, *21*, 084204.
(52) Sanville, E.; Kenny, S. D.; Smith, R.; Henkelman, G. Improved Grid-Based Algorithm for Bader Charge Allocation. *J. Comput. Chem.* **2007**, *28*, 899−908.
(53) Henkelman, G.; Arnaldsson, A.; Jónsson, H. A Fast and Robust Algorithm for Bader Decomposition of Charge Density. *Comp. Mater. Sci.* **2006**, *36*, 354−360.
(54) Yu, M.; Trinkle, D. R. Accurate and Efficient Algorithm for Bader Charge Integration. *J. Chem. Phys.* **2011**, *134*, 064111.
(55) Guo, Y.; Pan, F.; Ye, M.; Wang, Y.; Pan, P.; Zhang, X.; Li, J.; Zhang, H.; Lu, J. Interfacial Properties of Stanene−Metal Contacts. *2D Mater.* **2016**, *3*, 035020.
(56) Wang, Y.; Ye, M.; Weng, M.; Li, J.; Zhang, X.; Zhang, H.; Guo, Y.; Pan, Y.; Xiao, L.; Liu, J.; et al. Electrical Contacts in Monolayer Arsenene Devices. *ACS Appl. Mater. Interfaces* **2017**, *9*, 29273−29284.
(57) Ji, X.; Zhang, J.; Wang, Y.; Qian, H.; Yu, Z. A Theoretical Model for Metal-Graphene Contact Resistance Using a DFT-NEGF Method. *Phys. Chem. Chem. Phys.* **2013**, *15*, 17883−17886.
(58) Li, J.; Sun, X.; Xu, C.; Zhang, X.; Pan, Y.; Ye, M.; Song, Z.; Quhe, R.; Wang, Y.; Zhang, H.; et al. Electrical Contacts in Monolayer Blue Phosphorene Devices. *Nano Res.* **2018**, *11*, 1834.
(59) Pan, Y.; Dan, Y.; Wang, Y.; Ye, M.; Zhang, H.; Quhe, R.; Zhang, X.; Li, J.; Guo, W.; Yang, L.; et al. Schottky Barriers in Bilayer Phosphorene Transistors. *ACS Appl. Mater. Interfaces* **2017**, *9*, 12694−12705.
(60) Zhang, X.; Pan, Y.; Ye, M.; Quhe, R.; Wang, Y.; Guo, Y.; Zhang, H.; Dan, Y.; Song, Z.; Li, J.; et al. Three-Layer Phosphorene-Metal Interfaces. *Nano Res.* **2018**, *11*, 707−721.
(61) Mönch, W. Role of Virtual Gap States and Defects in Metal-Semiconductor Contacts. *Phys. Rev. Lett.* **1987**, *58*, 1260−1263.
(62) Mönch, W. Metal-Semiconductor Contacts: Electronic Properties. *Surf. Sci.* **1994**, *299−300*, 928−944.
(63) Guo, Y.; Pan, F.; Ye, M.; Sun, X.; Wang, Y.; Li, J.; Zhang, X.; Zhang, H.; Pan, Y.; Song, Z.; et al. Monolayer Bismuthene-Metal Contacts: A Theoretical Study. *ACS Appl. Mater. Interfaces* **2017**, *9*, 23128−23140.
(64) Kim, C.; Moon, I.; Lee, D.; Choi, M. S.; Ahmed, F.; Nam, S.; Cho, Y.; Shin, H.-J.; Park, S.; Yoo, W. J. Fermi Level Pinning at Electrical Metal Contacts of Monolayer Molybdenum Dichalcogenides. *ACS Nano* **2017**, *11*, 1588−1596.

DOI: 10.1021/acs.jpcc.8b03308
J. Phys. Chem. C 2018, 122, 12322−12331

(65) Gong, C.; Colombo, L.; Wallace, R. M.; Cho, K. The Unusual Mechanism of Partial Fermi Level Pinning at Metal-Mos_2 Interfaces. *Nano Lett.* **2014**, *14*, 1714−1720.

DOI: 10.1021/acs.jpcc.8b03308
J. Phys. Chem. C 2018, 122, 12322−12331